Size Dependence of Protein Diffusion Very Close to Membrane Surfaces: Measurement by Total Internal Reflection with Fluorescence Correlation Spectroscopy

Jamie K. Pero, Emily M. Haas, and Nancy L. Thompson*

Department of Chemistry, Campus Box 3290, University of North Carolina at Chapel Hill, Chapel Hill, North Carolina 27599-3290

Received: December 1, 2005; In Final Form: March 27, 2006

The diffusion coefficients of nine fluorescently labeled antibodies, antibody fragments, and antibody complexes have been measured in solution very close to supported planar membranes by using total internal reflection with fluorescence correlation spectroscopy (TIR-FCS). The hydrodynamic radii (3−24 nm) of the nine antibody types were determined by comparing literature values with bulk diffusion coefficients measured by spot FCS. The diffusion coefficients very near membranes decreased significantly with molecular size, and the size dependence was greater than that predicted to occur in bulk solution. The observation that membrane surfaces slow the local diffusion coefficient of proteins in a size-dependent manner suggests that the primary effect is hydrodynamic as predicted for simple spheres diffusing close to planar walls. The TIR-FCS data are consistent with predictions derived from hydrodynamic theory. This work illustrates one factor that could contribute to previously observed nonideal ligand−receptor kinetics at model and natural cell membranes.

Introduction

The interactions of ligands with their receptors at biological interfaces such as membranes are at the heart of many if not all biological processes including, for example, neurotransmission,[1] immunological response,[2] and nutrient uptake.[3] Previous studies have indicated that the association/dissociation kinetics of ligands in solution with receptors in natural or model membranes are very often not adequately explained as simple, reversible, bimolecular reactions between point particles.[4−9] Numerous hypotheses have been developed to account for the observed nonideality including models with an increased number of discrete states[10] or models in which the system is described as containing a continuum of bound states.[11−13] Other investigations into the molecular details of ligand−receptor kinetics have included rebinding effects[14−15] and rotational mobility or orientational effects.[16−17] An additional possibility is that the observed nonideality arises at least in part from deviations of the ligand translational mobility in close proximity to membranes from the bulk diffusion coefficient.

Total internal reflection with fluorescence correlation spectroscopy (TIR-FCS) is a method particularly well-suited to probing molecular motions and interactions close to surfaces. In TIR-FCS, a laser beam is internally reflected at the interface of a planar surface and an aqueous medium. The internal reflection generates a surface-associated evanescent field that penetrates only slightly into the aqueous medium and excites fluorescence from molecules bound to the surface or in solution but very close to the surface. The fluorescence arising from a small surface-adjacent volume, defined by the depth of the evanescent field along with an image-plane aperture, is monitored and fluctuates as molecules move into and out of the volume. The time dependence of the autocorrelation function of the fluorescence fluctuations provides information about the local translational mobility of the fluorescent molecules and, if they reversibly interact with surface sites, the kinetics associated with the surface interaction.

The theoretical basis for using TIR-FCS to examine near-surface dynamics, including translational diffusion in solution very close to the surface as well as the kinetics of reversible association and dissociation with the surface, has been established.[18−20] A number of experimental TIR-FCS studies have also been carried out. Initially, TIR-FCS was used to examine the reversible kinetics of tetramethylrhodamine-labeled immunoglobulin and insulin interacting with fused silica coated with serum albumin[21] and of rhodamine 6G interacting with C-18-modified silica surfaces.[22−23] Subsequently, a comprehensive set of measurements employed TIR-FCS to investigate molecular transport in substrate-supported, sol−gel films.[24−26] Two recent studies monitored the diffusion of fluorescein within the evanescent wave using TIR-FCS.[27−28] The first demonstration of TIR-FCS as a method for monitoring the kinetics of a specific and reversible association between fluorescently labeled ligands (IgG) in solution and their receptors (mouse FcγRII) embedded in substrate-supported planar membranes has been recently described.[29] Versions of TIR-FCS have also been used to monitor the motions of fluorescently labeled, intracellular vesicles near the plasma membranes of adherent cells.[30−31]

The work described here addresses the nature of protein diffusion very near model phospholipid membrane surfaces. The question considered is the manner in which the membrane affects local protein diffusion and therefore might affect the kinetics of interaction between protein ligands and their membrane-associated receptors. In a previous work, comprehensive TIR-FCS measurements were carried out for monoclonal mouse IgG diffusing close to substrate-supported planar model membranes.[32] The main conclusion of this work was that if local electrostatic fields significantly affect protein diffusion close to membrane surfaces, then the effects are confined to distances much smaller than 100 nm from the surface. However, this work did suggest that hydrodynamic effects might affect protein mobility close to membrane surfaces in a manner that might be

* Author to whom correspondence should be addressed. Phone: (919) 962-0328. Fax: (919) 966-3675. E-mail: nlt@unc.edu.

10.1021/jp056990y CCC: $33.50
Published on Web 05/17/2006

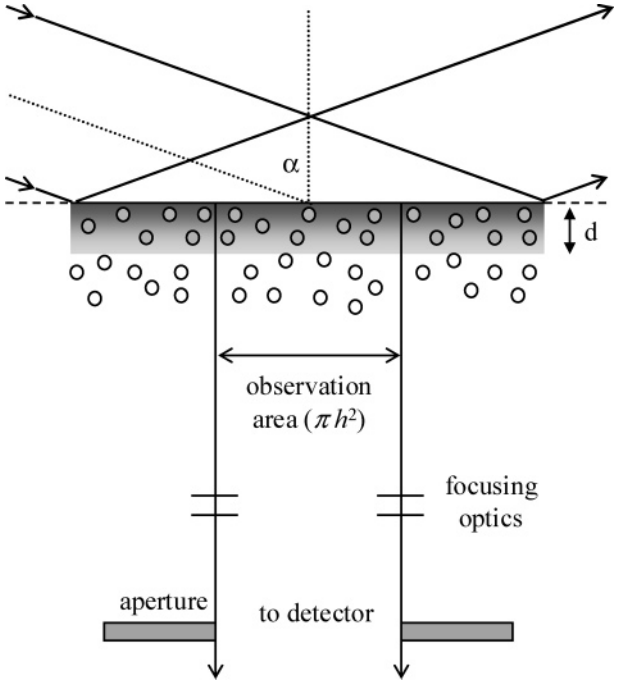

Figure 1. Total internal reflection with fluorescence correlation spectroscopy. A small sample volume is defined by the depth of the evanescent intensity, *d*, in combination with a circular aperture placed at an intermediate image plane of the microscope that defines an area of radius *h* in the sample plane. The fluorescence measured from the small sample volume adjacent to the surface fluctuates with time as molecules diffuse close to the surface, and the fluorescence fluctuations are autocorrelated.

observable even at distances extending 100 nm or more from the membrane.

Indeed, there exists a long-lived literature describing decreased diffusion of spherical particles close to planar walls. The core of these theories is related to the development of the notion of frictional coefficients when addressing macromolecular hydrodynamics. In these continuum-based theoretical treatments, the frictional coefficients for sphere motion through a viscous medium close to and both tangential or normal to the surface are increased, and the diffusion coefficients are decreased. These effects, for spheres diffusing close to walls, have been theoretically predicted for decades, and the signature is an increased dependence of the local diffusion coefficient on the size of the sphere.[33−35] The theoretical predictions have been experimentally verified, in part, for large colloidal particles.[36−43]

In the work described herein, the diffusion coefficients of nine fluorescently labeled antibody fragments, antibodies, and antibody complexes (with hydrodynamic radii ranging from 3 to 24 nm) adjacent to planar supported model membranes were measured by using TIR-FCS. The results show that the local diffusion coefficient decreases with the hydrodynamic radius, over and above that predicted by the Stokes−Einstein equation describing diffusion in bulk solution, and in a manner consistent with theoretical predictions according to hydrodynamic theories describing particle motions next to walls.

Theoretical Background

Apparatus. A laser beam is internally reflected at a substrate/solution interface and creates an evanescent intensity that penetrates exponentially with characteristic depth *d* into the solution adjacent to the surface[44,45] (Figure 1). The evanescent intensity, $I(z)$, is given by

$$I(z) = I_0 \exp\left(-\frac{z}{d}\right) \tag{1}$$

where *z* is the distance in solution from the interface. In the measurements described here, the interface of a fused silica substrate (refractive index $n_1 = 1.467$) and an aqueous salt solution (refractive index $n_2 \approx 1.337$)[32] is illuminated by a 488.0 nm laser line. For these refractive indices, the critical angle for internal reflection is $\alpha_C = 65.7°$. Thus, the incidence angle can in practice range from $\alpha \approx 71°$ to $\alpha \approx 85°$. For these conditions, the evanescent depth ranges from $d \approx 105$ nm to $d \approx 65$ nm. Fluorescence is collected through a 60×, 1.4 N.A. objective. The evanescent intensity along with a small circular aperture (50 μm radius) placed at an intermediate image plane of a microscope, corresponding to a radius $h \approx 1$ μm in the sample plane, defines a small observation volume.

Fluorescence Fluctuation Autocorrelation Function $G(\tau)$. Individual fluorescent molecules in solution diffuse into and out of the defined observation volume. Their motion causes the measured fluorescence to fluctuate with time. These fluctuations are defined as the difference between the instantaneous fluorescence intensity, $F(t)$, and its time-averaged value, $\langle F\rangle$; i.e., $\delta F(t) = F(t) - \langle F\rangle$. The fluorescence fluctuations are autocorrelated to obtain information about the diffusion of fluorescent molecules in the observation volume. The fluorescence fluctuation autocorrelation function is defined as

$$G(\tau) = \frac{\langle \delta F(t+\tau)\delta F(t)\rangle}{\langle F\rangle^2} = \frac{\langle \delta F(\tau)\delta F(0)\rangle}{\langle F\rangle^2} \tag{2}$$

Magnitude of the Fluorescence Fluctuation Autocorrelation Function. As shown previously,[19] if the concentration of fluorescent molecules in solution does not depend on *z*, as we assume here, then the magnitude of the fluorescence fluctuation autocorrelation function is

$$G_e(0) = \frac{1}{2N_e} \tag{3}$$

where N_e is the average number of fluorescent molecules in the observed volume, defined here as

$$N_e = \pi h^2 dA \tag{4}$$

$G_e(0)$ is inversely related to the solution concentration *A*.

Shape of the Fluorescence Fluctuation Autocorrelation Function for Spatially Independent Diffusion. In this work, we assume that the sample volume radius along the surface, *h*, is much greater than the evanescent depth, *d*. When the diffusion coefficient, *D*, does not depend on *z*, the theoretical form of the TIR-FCS fluorescence fluctuation autocorrelation function is[19]

$$G_e(\tau) = G_e(0)\left\{(1 - 2R_e\tau)\exp(R_e\tau)erfc[(R_e\tau)^{1/2}] + 2\left(\frac{R_e\tau}{\pi}\right)^{1/2}\right\} \tag{5}$$

where

$$R_e = \frac{D}{d^2} = \frac{\gamma}{d^2 r} \quad \text{and} \quad \gamma = \frac{kT}{6\pi\eta} \tag{6}$$

Here, R_e is the rate for diffusion in solution through the depth of the evanescent intensity, *r* is the hydrodynamic radius, *k* is Boltzmann's constant, *T* is the absolute temperature, and η is

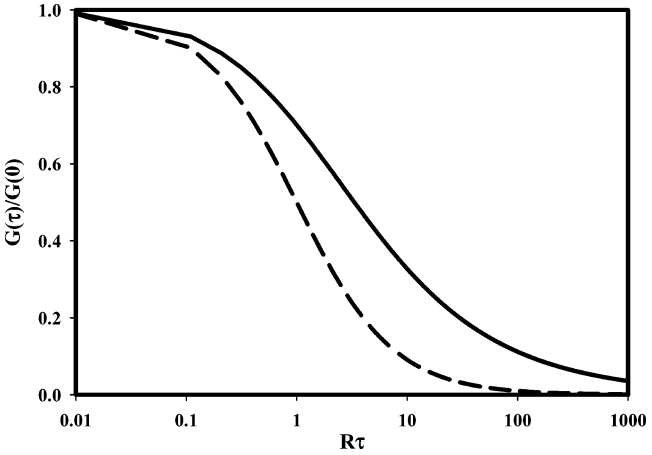

Figure 2. Fluorescence fluctuation autocorrelation function for spatially independent diffusion. $G(\tau)/G(0)$ decays with time. The solid line shows $G_e(\tau)/G_e(0)$ for evanescent illumination (eq 5). In this case, the initial slope is $-R_e$, and the half-time for decay is $3.3R_e^{-1}$. The dashed line shows $G_s(\tau)/G_s(0)$ for illumination with a focused spot in solution (eq 12). In this case, the initial slope is $-R_s$, and the half-time for decay is R_s^{-1}.

the solution viscosity. As shown in Figure 2a, $G_e(\tau)/G_e(0)$ decays monotonically with time. The magnitude of the initial slope is[46]

$$S_e = \left|\left\{\frac{d}{d\tau}\left[\frac{G_e(\tau)}{G_e(0)}\right]\right\}_{\tau=0}\right| = R_e \tag{7}$$

The time at which $G_e(\tau)$ equals one-half of its initial value is $3.3R_e^{-1}$.

Spatially Dependent Diffusion Coefficients. In this work, we are particularly concerned with the situation in which the diffusion coefficient depends on the distance from the interface. We test the hypothesis that the diffusion coefficient of proteins near membrane surfaces is significantly slowed by hydrodynamic effects. In this case, even in the absence of local potentials, this coefficient is predicted to depend on z (and the sphere radius, denoted here by r) for a sphere diffusing next to a wall. The predicted form of $D(z,r)$, for diffusional motion normal to the interface, is[3,38,43]

$$\frac{D}{D(z,r)} = \frac{4}{3}\sinh\left[\cosh^{-1}\left(1+\frac{z}{r}\right)\right]\sum_{k=1}^{\infty}\frac{k(k+1)}{(2k-1)(2k+3)}$$
$$\left\{\frac{2\sinh\left[(2k+1)\cosh^{-1}\left(1+\frac{z}{r}\right)\right]+(2k+1)\sinh\left[2\cosh^{-1}\left(1+\frac{z}{r}\right)\right]}{4\sinh^2\left[(k+0.5)\cosh^{-1}\left(1+\frac{z}{r}\right)\right]-(2k+1)^2\sinh^2\left[\cosh^{-1}\left(1+\frac{z}{r}\right)\right]}-1\right\} \tag{8}$$

where r is the particle radius, z is the distance between the sphere edge and the wall, and $D(\infty,r) = D$ is the diffusion coefficient in the bulk far from the wall. A much simpler, approximate form for eq 8 has been reported[42] as

$$\frac{D(z,r)}{D} = \frac{6z^2+2rz}{6z^2+9rz+2r^2} \tag{9}$$

Numerical calculations show that eqs 8 and 9 deviate by no more than 0.6%. The function $D(z,r)/D$, which ranges from zero to one as a function of z, is shown in Figure 3a.

Shape of the Fluorescence Fluctuation Autocorrelation Function for Spatially Dependent Diffusion. The generalization of eq 5 for the case in which the diffusion coefficient depends on z is not known. However, as shown in the Appendix, if $D(0) = 0$ (see eq 9), then the magnitude of the initial slope of the normalized fluorescence fluctuation autocorrelation function is

$$S_e(r) = R_e\left|\left\{\frac{\int_0^{\infty}\exp\left(-\frac{2z}{d}\right)\frac{D(z,r)}{D}\,dz}{\int_0^{\infty}\exp\left(-\frac{2z}{d}\right)dz}\right\}\right| \tag{10}$$

where R_e is given by eq 6. The value of S_e/R_e was calculated numerically from eqs 9 and 10 and is shown in Figure 3b. The ratio S_e/R_e decreases for larger particle radii and for thinner evanescent wave depths. Remarkably, S_e is predicted to be measurably less than that for pure bulk diffusion, R_e, even in cases where the particle radius is significantly less than the evanescent wave depth.

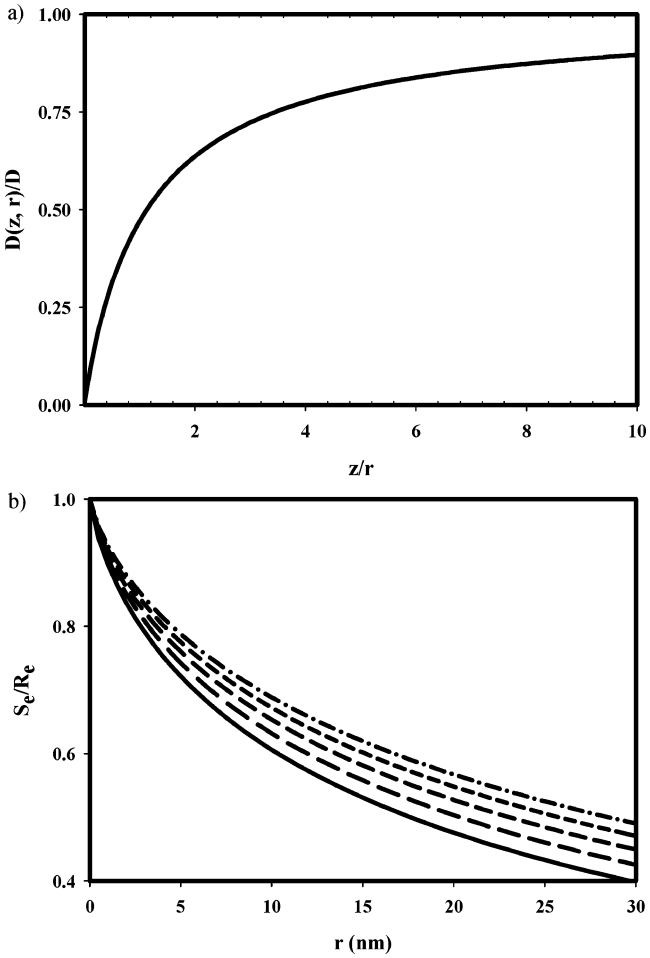

Figure 3. Distance-dependent diffusion for a sphere near a wall. (a) The diffusion coefficient as a function of the sphere radius r and the distance from the wall z increases from zero at the wall to the bulk diffusion coefficient as z approaches infinity. This plot was calculated from eq 9 and also equals eq 8. The distance for which $D(z,r) = (1/2)D$ is $z/r = (5 + 73^{1/2})/12 = 1.13$. (b) The value of eq 10 (with eq 9), calculated numerically, is shown for particle radii ranging from $0 \le r \le 30$ nm and for evanescent depths of (line) $d = 65$ nm, (long dash) $d = 75$ nm, (intermediate dash) $d = 85$ nm, (short dash) $d = 95$ nm, and (dash−dot) $d = 105$ nm. The effect on S_e/R_e is more prominent for larger radii and thinner evanescent wave depths.

Fluorescence Correlation Spectroscopy with a Focused Spot in Solution. In some measurements, the bulk diffusion coefficients of different protein preparations were examined by carrying out fluorescence correlation spectroscopy far from the

membrane surface. In these measurements, the sample volume was defined by tightly focusing the laser beam and aligning a confocal pinhole in a back image plane. In this case[47]

$$G_s(0) = \frac{1}{N_s} \tag{11}$$

where N_s is the average number of molecules in the new sample volume. The shape of the fluorescence fluctuation autocorrelation function is approximated as (see Materials and Methods section)

$$G_s(\tau) \approx \frac{G_s(0)}{1 + R_s\tau} \tag{12}$$

where

$$R_s = \frac{4D}{s^2} = \frac{4\gamma}{s^2 r} \tag{13}$$

s is the $1/e^2$ radius of the focused spot, and γ is defined in eq 6 (Figure 2b). The magnitude of the initial slope is

$$S_s = \left|\left\{\frac{d}{d\tau}\left[\frac{G_s(\tau)}{G_s(0)}\right]\right\}_{\tau=0}\right| = R_s \tag{13}$$

and the half-time for decay is R_s^{-1}.

Materials and Methods

Antibody Preparation. Antibodies of the type IgM (Sigma-Aldrich, St. Louis, MO), IgA (Sigma-Aldrich), IgG F(ab′)$_2$ (Jackson ImmunoResearch Laboratories, Inc., West Grove, PA), and IgG Fab (Jackson ImmunoResearch Laboratories) were dialyzed into phosphate-buffered saline (PBS; 0.05 M sodium phosphate, 0.15 M NaCl, pH 7.4). IgG antibodies were obtained from the anti-dinitrophenyl mouse−mouse hybridoma 1B711 (American Type Culture Collection, Rockville, MD), the anti-rat IgG mouse−mouse hybridoma MAR18.5 (American Type Culture Collection), and the anti-Thy-1 rat−mouse hybridoma 31-11 (Gerald J. Spangrude, University of Utah, Salt Lake City). Hybridomas were maintained in culture, and the secreted antibodies were purified from cell supernatants by affinity chromatography with dinitrophenyl-conjugated human serum albumin for 1B711 antibodies,[32] with protein G for MAR18.5 antibodies, and with MAR18.5 for 31-11 antibodies.[48] For MAR18.5 purification, the wash buffer was PBS, and the elution buffer was 0.1 M glycine, 0.01% NaN_3, pH 2.7. Each liter of supernatant yielded approximately 10−15 mg of antibody as determined spectrophotometrically by assuming that the molar absorptivity at 280 nm was 1.4 mL mg^{-1} cm^{-1}. All antibodies were subjected to sodium dodecyl sulfate polyacrylamide gel electrophoresis (SDS-PAGE) with silver staining and fast protein liquid chromatography (FPLC)−dynamic light scattering to ascertain their purity.

Covalently conjugated antibody complexes (AbCs) were engineered to make molecules of differing radii than those found naturally and provide a broader range of molecular sizes to study. The 31-11 antibodies were mixed with the MAR18.5 antibodies at a 2:1 ratio as an MAR18.5 antibody can in principle bind two 31-11 antibodies on their light chains. After the antibodies were mixed the final antibody concentration ranged between 3 and 10 mg/mL in PBS. Bis(sulfosuccinimidyl) suberate (BS^3) (Pierce Biotechology, Rockford, IL) was then added to the antibodies in a 20−120 M excess to bind the antibodies together and prevent equilibrium dissociation. The reaction with BS^3 was carried out for 30 min and then quenched with 25−45 mM glycine, at room temperature. The mixture was then dialyzed against PBS at 4°C to remove excess glycine and BS^3.

The mixture of antibody complexes was then subjected to SDS-PAGE analysis with silver staining to determine the number of products formed. The gels indicated that a broad range of products had been created. This mixture of AbCs was dialyzed into PBS with 0.5 M NaCl and passed through a 0.2 μm filter. The AbCs were separated using an ÄKTA fast protein liquid chromatograph instrument interfaced with a Tricorn Superose 6 column (Amersham Biosciences, Piscataway, NJ). The FPLC separation was carried out at a flow rate between 0.4 and 0.5 mL/min, and 0.5 mL fractions were collected. Analysis of the chromatographic trace revealed that the separation was incomplete and produced one broad peak. Numerous separations were performed under the same conditions, and the eluents were pooled fraction by fraction. The broad peak was divided into five groups. The first of the five groups was discarded as it contained extremely large AbCs. The remaining four groups were dialyzed into PBS and named AbC1, AbC2, AbC3, and AbC4, with AbC1 being the largest and first to elute and AbC4 being the smallest and last to elute.

All antibodies and AbCs were fluorescently labeled using the AlexaFluor488 Protein Labeling Kit (Molecular Probes, Inc., Eugene OR). The free dye was removed by using size exclusion chromatography with Sephadex G-25 or G-50 in PBS. The molar concentrations of antibody or AbC and the molar ratios of AlexaFluor488 to antibody or AbC (0.5−9 dyes/protein) were determined spectrophotometrically according to the manufacturer's protocol. The molar extinction coefficients (in M^{-1} cm^{-1}) for the antibodies and antibody complexes were approximated by multiplying 1.4 L/cm g by the estimated molecular weights. The estimated molecular weights for the AbCs were determined by using a Wyatt DAWN EOS light scattering instrument interfaced to an Amersham Biosciences AKTA. As described above, the FPLC separation was incomplete. Consequently, the peak was split into five segments, the first segment was excluded, and the light scattering software was used to determine an average molecular weight for the remaining four segments. Immediately before use, Fab, F(ab′)$_2$, IgG, and AbC4 were clarified using 0.1 μm and then 0.02 μm filters; IgM, IgA, AbC1, AbC2, and AbC3 were clarified using 0.2 μm filters.

Phospholipid Vesicles. Small unilamellar vesicles of 1-palmitoyl-2-oleoyl-glycero-3-phosphocholine (POPC) (Avanti Polar Lipids, Birmingham, AL) were prepared by tip sonication of 2 mM suspensions of POPC in water as previously described.[49] In some experiments, 2 mol % of the fluorescent lipid 1-acyl-2-[12-(7-nitro-2-1,3-benzoxadiazol-4-yl) aminododecanoyl]-glycero-3-phophocholine (NBD-PC) was included to monitor bilayer formation and quality (see below). Vesicle suspensions were clarified by air ultracentrifugation (130 000*g*, 30 min) immediately before use.

Substrate-Supported Phospholipid Bilayers. Substrate-supported planar phospholipid bilayers were formed as previously described.[50] Fused silica substrates were cleaned extensively by boiling in detergent (ICN, Aurora, OH), bath-sonicating, rinsing thoroughly with deionized water, and drying at 160 °C. Substrates were cleaned in an argon ion plasma cleaner (15 min, 25 °C) (PDC-3XG, Harrick Scientific, Ossining, NY). Planar bilayers were formed by applying 75 μL of the vesicle suspension to a fused silica substrate (1 h, 25 °C) and rinsing with 3 mL of PBS. Fluorescence imaging microscopy and fluorescence pattern photobleaching recovery indicated that

bilayers containing NBD-PC were continuous and fluid. For TIR-FCS measurements, bilayers without NBD-PC were treated with 400 μL of 15−90 nM antibody or AbC in PBS. For FCS experiments with a focused spot, bilayers without NBD-PC were treated with a mixture of 3 nM antibody or AbC and 27 nM unlabeled antibody or AbC.

Fluorescence Microscopy. TIR-FCS and FCS with a focused spot were carried out on an instrument consisting of an argon ion laser (Innova 90-3; Coherent, Palo Alto, CA), an inverted microscope (Zeiss Axiovert 35), and a single-photon counting photomultiplier (RCA C31034A, Lancaster, PA). All experiments were conducted at 25 °C using the 488 nm laser line. For TIR-FCS measurements, the laser beam was s-polarized while incident on the fused silica/aqueous interface and generated an evanescent field polarized parallel to the interface. The incidence angle was ∼71−85°, corresponding to theoretically predicted evanescent wave depths ranging from 105 to 65 nm (see above). For conventional FCS measurements, the laser beam was focused in the protein solution approximately 20 μm from the bilayer surface to form a small Gaussian-shaped illumination with a radius on the order of $s \approx 1$ μm.

In both TIR-FCS and focused beam experiments, a pinhole with a radius of 50 μm placed at an internal image plane defined an area with a radius of $h \approx 1$ μm when projected onto the sample plane. The fluorescence arising from the volume defined by the excitation light and the pinhole was collected through a 60×, 1.4 N.A. objective. The fluorescence signal was autocorrelated by a PC-based correlator board (model 5000/E, ALV). Autocorrelation functions were obtained within 5−10 min using incident laser intensities of 4−17 μW/μm^2 for TIR-FCS experiments or 5−30 μW/μm^2 for FCS experiments using the focused beam. The resulting evanescent intensities at the interface differed by a factor of ∼0.2−2.5.[51] Average blank signals were measured from samples containing buffer adjacent to supported bilayers. Possible detector afterpulsing was examined by using a published procedure.[52] The measurements demonstrated that any afterpulsing present was extremely minimal and in any case much faster than the time range of the TIR-FCS data (Figure 4).

Data Analysis. Autocorrelation functions were background-corrected by multiplying by the factor $\langle S\rangle^2/\langle F\rangle^2$, where $\langle F\rangle = \langle S\rangle - \langle B\rangle$ was the average fluorescence calculated by subtracting the average measured blank signal $\langle B\rangle$ from the average measured total signal $\langle S\rangle$.[47] TIR-FCS autocorrelation functions were fit to eq 5 with eq 3 plus an arbitrary constant G_∞, and the free parameters were R_e, N_e, and G_∞. Autocorrelation functions measured using the focused beam were fit to eq 12 with eq 11 plus an arbitrary constant G_∞, and the free parameters were R_s, N_s, and G_∞. For spot FCS measurements, the more general expression, $G_s(\tau) \approx G_s(0)[1 + R_s\tau]^{-1}[1 + (R_s\tau/\sigma^2)]^{-1/2}$, where σ is the "structure parameter", may also be used for data analysis. However, the value of σ in our apparatus is approximately 3, and the second factor in the more general expression is negligible.[53]

Results

As viewed through a 1.4 N.A. objective using evanescent illumination, samples consisting of soluble antibodies or AbCs near planar model POPC membranes displayed visually apparent fluorescence fluctuations that appeared as fluorescent twinkles against a uniform background. The temporal fluctuations in fluorescence, as measured through a small pinhole at a back image plane (Figure 1), were autocorrelated (eq 2). These TIR-FCS measurements were carried out for nine antibodies or AbCs.

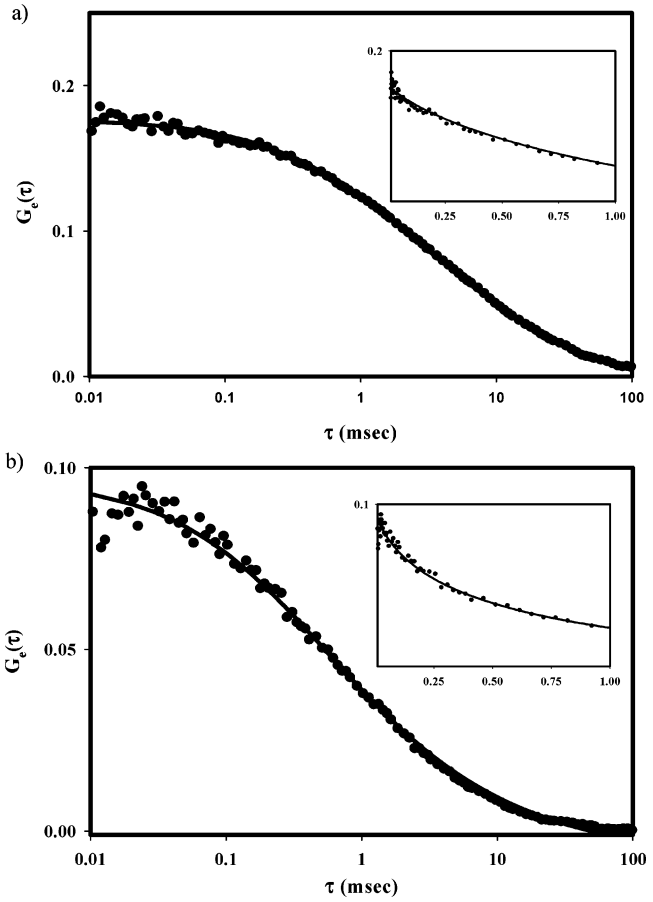

Figure 4. Representative TIR-FCS autocorrelation functions. The background-corrected $G_e(\tau)$ are for (a) AbC1 or (b) AbC4 in PBS adjacent to a POPC membrane. The fluorescence was monitored and autocorrelated for 300 s. The average signals $\langle S\rangle$ and background intensities $\langle B\rangle$ were (a) 10.61 and 0.04 kHz and (b) 10.03 and 0.19 kHz. The best fits of these particular functions to eq 5 with eq 3 gave (a) $N_e = 2.55$, $R_e = 0.826$ ms^{-1} and (b) $N_e = 4.81$, $R_e = 4.51$ ms^{-1}. Note that the theoretical curves accurately find the initial slope (insets).

Correlation functions for matched samples not containing fluorescent solutes were not measurable.

Background-corrected TIR-FCS autocorrelation functions, $G_e(\tau)$, were fit to eq 5 (with eq 3) plus an arbitrary constant G_∞, with free parameters N_e, R_e, and G_∞. Typical experimentally obtained $G_e(\tau)$ functions and their best fits to this theoretical form, for two of the nine samples, are shown in Figure 4. The best-fit values of the arbitrary offset, G_∞, were on the average less than ∼10% in magnitude compared to the best-fit values of $G_e(0)$. The best-fit values of N_e ranged from ∼2 to 20, consistent with the expected values of N_e for solution concentrations $A = 15-90$ nM, an evanescent wave depth $d = 85$ nm (see below), and an observation area radius $h = 1.0$ μm (eq 4). The best-fit values of R_e ranged from 7.8 to 0.8 ms^{-1} and decreased systematically with molecular size, consistent with expectations. To ensure that the TIR-FCS data did not show photoartifacts, the incident intensity was kept between 4 and 17 μW/μm^2,[32] and $G_e(\tau)$ functions were measured for at least two different incident intensities. No significant change in the best-fit parameters was observed for the two different intensities.

In principle, eq 5 does not describe the precise shape of the autocorrelation function when the diffusion coefficient depends on the distance from the surface (see above). The form of this function is unknown, but the magnitude of its initial slope S_e is predicted by eq 10 (Appendix). Thus, it is important to note that the best fits of the experimental autocorrelation functions

TABLE 1: Hydrodynamic Radii[a]

protein	hydrodynamic radius (nm)
IgG Fab	2.91[b]
IgG $(Fab')_2$	4.48[b]
IgG	5.29[b]
IgA	6.92[c]
IgM	12.65[b]
AbC4	4.73[c]
AbC3	6.60[c]
AbC2	12.98[c]
AbC1	23.73[c]

[a] Diffusion rates in bulk solution, R_s, were determined for all nine molecule types by using conventional FCS with a spot focused far from the membrane surface. [b] IgG Fab, IgG $(Fab')_2$, IgG, and IgM radii are from the literature.[54] The average measured values of R_s for these four molecules were plotted against the reciprocal of their radii and used to find a best- fit value for the constant $4\gamma s^{-2}$ (eqs 6 and 13). [c] The best-fit value of this constant was used with eq 13 to determine the radii r for the remaining five molecules, IgA and AbC1−4.

to eq 5 accurately find the initial slope (Figure 4), upon which further analysis is based. Both the magnitude of the initial slope S_e and the characteristic time for decay of eq 5 are equal to R_e (eqs 6 and 7).

Conventional FCS measurements with a focused spot were carried out in solutions adjacent but not close to planar membranes, on each of the nine sample types, to determine the hydrodynamic radii of the AbC molecules and the IgA molecule. These autocorrelation functions were background-corrected, and the resulting functions $G_s(\tau)$ were fit to eq 12 (with eq 11) plus an arbitrary constant G_∞, with free parameters N_s, R_s, and G_∞. Hydrodynamic radii for IgG Fab, IgG $(Fab')_2$, IgG, and IgM were taken from the literature.[54] The literature value for the IgA radius was not included because it was for monomeric IgA, and dynamic light scattering measurements (see Materials and Methods section) indicated that the IgA used here was dimeric and trimeric in form. At room temperature in aqueous solution, $\gamma \approx 218\ \mu m^2\ nm\ s^{-1}$ (eq 6). Linear regression of the measured values of R_s as a function of the inverse of the four literature values of r (eq 13) implied $4\gamma s^{-2} = 793.9\ nm\ s^{-1}$, consistent with a (reasonable) s value of $\sim 1\ \mu m$. The constant $4\gamma s^{-2}$ was then used with the other measured values of R_s and eq 13 to determine the radii of the AbCs and IgA (Table 1).

For the three molecules with the smallest literature-derived molecular radii (Fab, $(Fab')_2$, and IgG) there should be only small surface effects, and their bulk diffusion coefficients can be estimated by using the measured values of R_e and $D = R_e d^2$ (eq 6). For evanescent wave depths ranging from 80 to 90 nm, these calculations implied D values of 50−63, 36−45, and 29−37 $\mu m^2\ s^{-1}$, respectively. These values are in good agreement with expectations (i.e., slightly lower than) the values predicted by $D = \gamma r^{-1}$ (eq 6) and the hydrodynamic radii given in Table 1, which are 75, 49, and 41 $\mu m^2\ s^{-1}$.

The average best-fit values of R_e ($= S_e$) for each of the nine sample types are shown as a function of the hydrodynamic radius in Figure 5a. As expected, S_e decreased significantly with increasing molecular size. In addition, the S_e values agreed very well with the values predicted by eqs 6, 9, and 10. These predicted values are also shown in Figure 5a, for $\gamma = 2.18 \times 10^5\ nm^3\ ms^{-1}$ and evanescent wave depths of $d = 75$, 85, and 95 nm.

Although there is good agreement between the measured and predicted values of S_e, a decrease in the bulk diffusion coefficient is predicted with molecular size, even in the absence of surface effects, by the Stokes−Einstein equation (eq 6). A more stringent

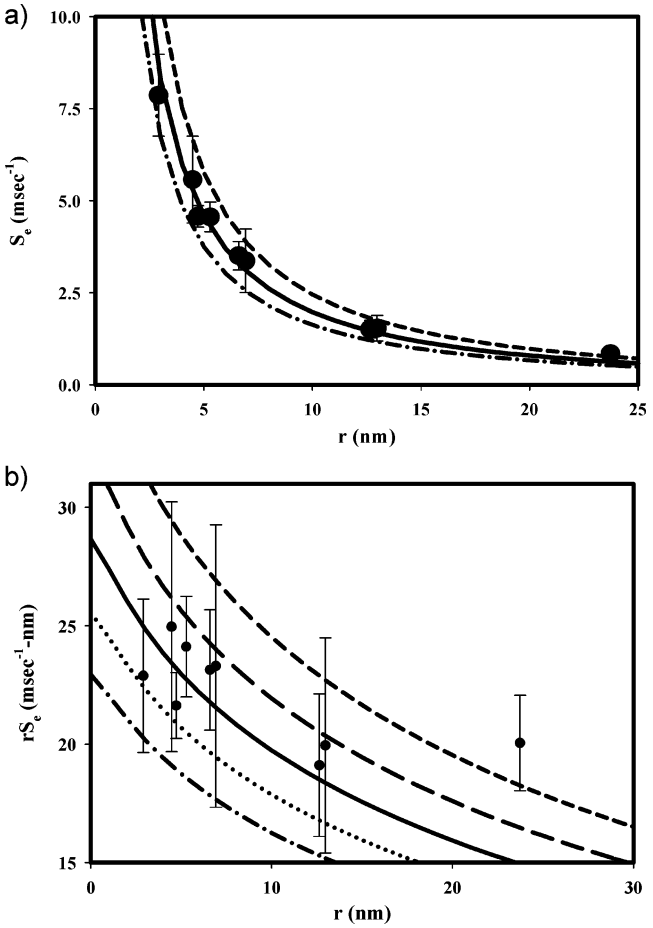

Figure 5. S_e and rS_e as a function of r. (a) The measured values of S_e decrease significantly with the hydrodynamic radius r. (b) The measured values of rS_e also decrease with r. In both parts a and b, each experimental point shows the average and standard deviation found from approximately 35 independently measured autocorrelation functions. These values are compared with theoretical predictions (eqs 6, 9, and 10 with $\gamma = 2.18 \times 10^5\ nm^3\ ms^{-1}$) for evanescent wave depths d equal to (short dash) 75 nm, (long dash) 80 nm, (line) 85 nm, (dot) 90 nm, and (dash−dot) 95 nm.

test for the presence of surface effects is to remove the influence of the Stokes−Einstein equation and question if the values of S_e still decrease with molecular radius; i.e., to question if the product rS_e decreases with r. In the absence of surface effects, $S_e = \gamma(rd^2)^{-1}$ is predicted to be inversely proportional to r and $rS_e = \gamma d^{-2}$ to be independent of r. Figure 5b shows the measured values of the product rS_e as a function of r. Although the values of the standard deviations of these products relative to the average product magnitudes are ∼15%, the average product values themselves do not strictly monotonically decay, although overall, rS_e appears to decrease with r. (A possible source of noise in the relative average values of the products was day-to-day variability in the incidence angle and therefore evanescent wave depth).

To determine statistically whether rS_e in fact decreased with r, linear regression analyses with four data sets were carried out: (1) the nine average values of rS_e versus r shown in Figure 5b; (2) the first eight average values of rS_e versus r shown in Figure 5b (because the last point, for AbC1, seemed not to be as low as one might predict); (3) the 312 individual values of rS_e used to construct the nine average values of rS_e shown in Figure 5b; and (4) the 290 individual values of rS_e used to construct the first eight average values of rS_e shown in Figure 5b. The results of these analyses are as follows, where α denotes

the intercept, β denotes the slope, and R denotes the correlation coefficient: (1) $\alpha = 24.1$ nm ms^{-1}, $\beta = -0.225$ ms^{-1}, $R = 0.725$; (2) $\alpha = 25.5$ nm ms^{-1}, $\beta = -0.437$ ms^{-1}, $R = 0.814$; (3) $\alpha = 24.2$ nm ms^{-1}, $\beta = -0.255$ ms^{-1}, $R = 0.364$; and (4) $\alpha = 25.3$ nm ms^{-1}, $\beta = -0.425$ ms^{-1}, $R = 0.401$.

The most important question is whether the correlation coefficients R indicate a statistically significant decrease in the product rS_e with r. The probabilities p_1 that the correlation coefficients would be of their magnitude or greater, in the absence of a correlation between rS_e and r and given the number of data points included in the various sets, are as follows:[55] (1) $p_1 = 0.027$; (2) $p_1 = 0.014$; (3) $p_1 \ll 0.0001$; and (4) $p_1 \ll 0.0001$. The first two values of p_1 imply that the product rS_e most likely decreases with r. However, these cases are more stringent tests in that all of the data points are not included in the analysis. The last two values of p_1, which are found from the more accurate analysis, imply that the product rS_e almost certainly decreases with r. This result is the main conclusion of the work presented here: After accounting for the decrease in the diffusion coefficient in bulk as a function of molecular size, there remains a statistically significant decrease in the diffusion coefficient of proteins close to membrane surfaces that increases in strength with molecular size. The most likely explanation for this result is that it is a consequence of the predicted decrease in diffusion of particles close to walls due to hydrodynamic effects.

To evaluate the magnitudes of the intercepts α and slopes β, the theoretically predicted values of rS_e were calculated from eqs 6, 9, and 10 for the nine hydrodynamic radii shown in Table 1. These values were subjected to linear regression for six cases. The value of γ was assumed to be 2.18×10^5 nm^3 ms^{-1} (see above), and the evanescent wave depth d was assumed to equal 80, 85, or 90 nm. The first set of three fits were carried out for all nine r values and for the three assumed evanescent wave depths. These calculations implied intercepts α ranging from 23 to 28 nm ms^{-1} and slopes β ranging from -0.41 to -0.54 ms^{-1}. The second set of three fits was carried out for the first eight points and for evanescent wave depths equal to 80, 85, or 90 nm. These calculations implied intercepts α ranging from 23 to 29 nm ms^{-1} and slopes β ranging from -0.54 to -0.71 ms^{-1}. Thus, the measured values of the intercept, $\alpha = 24-25$ nm ms^{-1} (see above), agree extremely well with the predicted values. However, the measured values of the slope β do not have quite as good of an agreement with the theoretically predicted values. For the data sets containing all nine points, the theoretically predicted values (-0.41 to -0.54 ms^{-1}) are higher in magnitude than the experimental values (-0.23 to -0.26 ms^{-1}) by factors ranging from 1.6 to 2.3. For data sets containing only the first eight points, the theoretically predicted values (-0.54 to -0.71 ms^{-1}) are higher than the experimental values (-0.43 to -0.44 ms^{-1}) by factors ranging from 1.2 to 1.6. This result suggests that other factors may have contributed to the observed decrease in rS_e; however, agreement is still very good given the noise in the data.

Figure 5b shows the measured values of rS_e as a function of r, along with the theoretically predicted values numerically calculated from eqs 6, 9, and 10 with $\gamma = 2.18 \times 10^5$ nm^3 ms^{-1}. Given the statistical significance of the main conclusion that the product rS_e decreases with r, the agreement between the measured values of rS_e and the theoretically predicted values, with no adjustable parameters, is remarkable. As a final statistical test, weighted, reduced χ^2 values for comparing the measured and predicted values of rS_e were calculated as a function of the evanescent wave depth ($d = 70$, 75, 85, 90, and 95 nm) and by including all nine or the first eight points. In both cases, χ^2 was minimized at $d = 85$ nm. For all nine points, the minimum value of χ^2 was 1.02, and for the first eight points, the minimum value of χ^2 was 0.34. The probabilities p_2 of finding χ^2 values equal to or larger than the determined ones, given that the data are well-described by the theory, were calculated to equal 0.42 and 0.95, respectively. These values of p_2 are well above the conventional value (≤ 0.05) for which it is concluded that significant disagreement exists between data and theoretical predictions.[55] Therefore, the statistical analysis confirms the visual impression that the data in Figure 5b agree well with the theoretical predictions.

Discussion

Although the parameters governing protein diffusion in homogeneous, aqueous solution are well-characterized,[34,56−62] very little is known about the manner in which cell membrane surfaces affect the diffusion of nearby proteins causing putative deviations from what one would expect in bulk solution. This question is of biological significance at least in part because of the role that diffusion can play in the kinetics of protein−protein interactions. If membrane surfaces significantly change the local diffusion properties of protein ligands, then the effects could govern the kinetics of ligand−receptor interactions and therefore associated cellular responses.

In a previous study, it was shown that TIR-FCS can be used to characterize protein diffusion very close to substrate-supported planar membranes.[32] In this work, TIR-FCS measurements were carried out for a model protein, monoclonal mouse IgG, for a variety of electrostatic conditions including membranes that were positively charged, negatively charged, or zwitterionic, for different solution pH values spanning the isoelectric point of the IgG, and for solutions with different ionic strengths. No statistically significant change in the local diffusion coefficient was observed for differently charged membranes or IgG molecules; however, the IgG diffusion did decrease somewhat with increasing ionic strength, suggesting that salt-induced changes in the IgG molecules might be changing the local diffusion coefficient indirectly through hydrodynamic effects.

In the work described here, the hypothesis that protein ligands close to membrane surfaces experience hydrodynamic reductions in diffusion was tested according to the primary signature of this predicted effect, that planar surfaces restrict the local diffusion of spherical particles in a manner that depends on the particle size. To do so, nine different proteins with similar chemical characteristics (i.e., all derived from antibodies) but different sizes were assembled (Table 1). As shown in Figure 5a, the local diffusion rate as measured by TIR-FCS decreased significantly with the molecular radius, as expected. As shown in Figure 5b, even after accounting for the decrease in the diffusion coefficient with the molecular radius that would be expected in bulk solution, the local diffusion coefficient still decreased with molecular size, consistent with the hydrodynamic hypothesis. Remarkably, (1) the data are entirely consistent with predictions for the manner in which a planar surface affects the local mobility of a spherical particle[33,38,42,43] (eqs 8 and 9), with no adjustable parameters included in the comparison of theory and data, and (2) the effects are long-range in that they are observable even at an evanescent wave depth of $d \approx 85$ nm. We therefore tentatively conclude that future reaction−diffusion models for cell-surface ligand−receptor interactions should account for these hydrodynamic effects on local ligand diffusion.

In future studies measurements carried out as a function of the incidence angle and therefore the evanescent wave depth

could provide additional confirmation of the observed effect. Opportunities also exist for using substrates with very high refractive indices (e.g., single-crystal TiO_2 or $SrTiO_3$) to create extremely thin evanescent waves (as low as 18 nm).[50] Equation 7 predicts that, in the absence of hydrodynamic effects, no reduction in the product rS_e will be observed. Much different results are expected in the presence of hydrodynamic effects, and the results are predicted to be more prominent for thinner evanescent waves (eq 10). Other possibly useful approaches include the use photon counting histograms[63] or high-order autocorrelation.[64]

It will also be important to carry out these measurements near natural cell membranes. For adherent, thick cells, TIR-FCS can in principle monitor the diffusion of cytoplasmic molecules close to the inner membrane leaflet.[65−66] This method is also likely to be adaptable to external ligands interacting with very thin extended regions of adherent cells where the double membrane and cellular interior are thin enough so that the evanescent wave extends through the entire cell to the outer leaflet of the apical cell membrane.

Acknowledgment. We thank Lisa Charlton, Julie Bryant, and Gary Pielak for assistance with the FPLC, Ashutosh Tripathy from the UNC Macromolecular Interactions Facility for assistance with the light scattering, and Gerald J. Spangrude of the University of Utah for 31-11 hybridomas. This work was funded by the National Science Foundation (Grant No. MCB-0130589).

Appendix: TIR-FCS Autocorrelation Function for Spatially Dependent Diffusion

As described previously[19]

$$\frac{G_e(\tau)}{G_e(0)} = \frac{2}{\langle A\rangle d}\int_0^\infty dz' \exp\left(-\frac{z'}{d}\right)\int_0^\infty dz \exp\left(-\frac{z}{d}\right)\varphi(z,z',\tau) \quad (A1)$$

where $\varphi(z,z',\tau)$ denotes the concentration fluctuation autocorrelation function; i.e.,

$$\varphi(z,z',\tau) = \langle \delta A(z,\tau)\delta A(z',0)\rangle \quad (A2)$$

$A(z,\tau)$ is the concentration at position z and time τ, $\langle A\rangle$ is the average concentration, and $\delta A(z,\tau) = A(z,\tau) - \langle A\rangle$ is the concentration fluctuation at position z and time τ. The partial differential equation describing the behavior of $\varphi(z,z',\tau)$, for spatially dependent diffusion, is[37]

$$\frac{\partial}{\partial \tau}\varphi(z,z',\tau) = \frac{\partial}{\partial z}\left[D(z)\frac{\partial}{\partial z}\varphi(z,z',\tau)\right] \quad (A3)$$

The boundary conditions are

$$[\varphi(z,z',\tau)]_{z=\infty} = 0$$

$$\left[\frac{\partial}{\partial z}\varphi(z,z',\tau)\right]_{z=0} = 0 \quad (A4)$$

and the initial condition is

$$[\varphi(z,z',\tau)]_{\tau=0} = \langle A\rangle\delta(z - z') \quad (A5)$$

where $\delta(z-z')$ is a Dirac delta function. Using eq A5 in eq A1 shows that $[G_e(\tau)/G_e(0)]_{\tau=0} = 1$. We calculate the initial slope as (see eqs 10, A1, and A3)

$$S_e = \frac{2}{\langle A\rangle d}\left\{\int_0^\infty dz' \exp\left(-\frac{z'}{d}\right) \times \int_0^\infty dz \exp\left(-\frac{z}{d}\right)\left[\frac{\partial}{\partial z}\left[D(z)\frac{\partial}{\partial z}\varphi(z,z',\tau)\right]\right]\right\}_{\tau=0} \quad (A6)$$

Evaluating the integral over the variable z by parts (twice) and using the condition that $D(0) = 0$ implies that

$$S_e = \frac{2}{\langle A\rangle d^2}\left\{\int_0^\infty dz' \exp\left(-\frac{z'}{d}\right) \times \int_0^\infty dz \exp\left(-\frac{z}{d}\right)\left[\frac{1}{d}D(z) - \frac{d}{dz}D(z)\right]\varphi(z,z',\tau)\right\}_{\tau=0} \quad (A7)$$

By using eq A5, one finds that

$$S_e = \frac{2}{d^2}\int_0^\infty dz' \exp\left(-\frac{2z'}{d}\right)\left[\frac{1}{d}D(z') - \frac{d}{dz'}D(z')\right] \quad (A8)$$

Evaluating the second integral by parts yields

$$S_e = \frac{2}{d^3}\int_0^\infty \exp\left(-\frac{2z'}{d}\right)D(z')\,dz' \quad (A9)$$

Equation A9 with eq 6 implies eq 10.

References and Notes

(1) Kim, J. H.; Huganir, R. L. *Curr. Opin. Cell Biol.* **1999**, *11*, 248.
(2) Ravetch, J. V.; Bolland, S. *Annu. Rev. Immunol.* **2001**, *19*, 275.
(3) Zorzano, A.; Fandos, C.; Palacin, M. *Biochem. J.* **2000**, *349*, 667.
(4) Hsieh, H. V.; Thompson, N. L. *Biochemistry* **1995**, *34*, 12481.
(5) Payne, M. A.; Igo, J. D.; Cao, Z. H.; Foster, S. B.; Newton, S. M.; Klebba, T. E. *J. Biol. Chem.* **1997**, *272*, 21950.
(6) McKiernan, A. E.; MacDonald, R. I.; MacDonald, R. C.; Axelrod, D. *Biophys. J.* **1997**, *73*, 1987.
(7) Anderson, T. G.; McConnell, H. M. *Biophys. J.* **1999**, *77*, 2451.
(8) Sahu, A.; Soulika, A. M.; Morikis, D.; Spruce, L.; Moore, W. T.; Lambirs, J. D. *J. Immunol.* **2000**, *165*, 2491.
(9) Domagala, T.; Konstantopoulos, N.; Smyth, F.; Jorissen, R. N.; Fabri, L.; Geleick, D.; Lax, I.; Schlessinger, J.; Sawyer, W.; Howlett, G. F.; Burgess, A. W.; Nice, E. C. *Growth Factors* **2000**, *18*, 11.
(10) Lauffenburger, D. A.; Lindermann, J. J. *Receptors: Models for Binding, Trafficking, and Signaling*; Oxford University Press: Oxford, United Kingdom, 1993.
(11) Kopelman, R. *Science* **1988**, *241*, 1620.
(12) Frauenfelder, H.; Sligar, S. G.; Wolynes, P. G. *Science* **1991**, *254*, 1598.
(13) Murray, D.; Honig, B. *Mol. Cell* **2002**, *9*, 145.
(14) Lagerholm, B. C.; Thompson, N. L. *Biophys. J.* **1998**, *74*, 1215.
(15) Levin, M. D.; Shimizu, T. S.; Bray, D. *Biophys. J.* **2002**, *82*, 1809.
(16) Shoup, D.; Lipari, G.; Szabo, A. *Biophys. J.* **1981**, *36*, 551.
(17) Schweitzer-Stenner, R.; Licht, A.; Pecht, I. *Biophys. J.* **1992**, *63*, 551.
(18) Thompson, N. L.; Burghardt, T. P.; Axelrod, D. *Biophys. J.* **1981**, *33*, 435.
(19) Starr, T. E.; Thompson, N. L. *Biophys. J.* **2001**, *80*, 1575.
(20) Lieto, A. M.; Thompson, N. L. *Biophys. J.* **2004**, *87*, 1268.
(21) Thompson, N. L.; Axelrod, D. *Biophys. J.* **1983**, *43*, 103.
(22) Hansen, R. L.; Harris, J. M. *Anal. Chem.* **1998**, *70*, 2565.
(23) Hansen, R. L.; Harris, J. M. *Anal. Chem.* **1998**, *70*, 4247.
(24) McCain, K. S.; Harris, J. M. *Anal. Chem.* **2002**, *75*, 3616.
(25) McCain, K. S.; Schluesche, P.; Harris, J. M. *Anal. Chem.* **2004**, *76*, 930.
(26) McCain, K. S.; Schluesche, P.; Harris, J. M. *Anal. Chem.* **2004**, *76*, 939.
(27) Harlepp, S.; Robert, J.; Darnton, N. C.; Chatenay, D. *Appl. Phys. Lett.* **2004**, *85*, 3917.
(28) Hassler, K.; Anhut, T.; Rigler, R.; Gösch, M.; Lasser, T. *Biophys. J.* **2005**, *88*, L1.
(29) Lieto, A. M.; Cush, R. C.; Thompson, N. L. *Biophys. J.* **2003**, *85*, 3294.
(30) Johns, L. M.; Levitan, E. S.; Shelden, E. A.; Holz, R. W.; Axelrod, D. *J. Cell Biol.* **2001**, *153*, 177.
(31) Holt, M.; Cooke, A.; Neef, A.; Lagnado, L. *Curr. Biol.* **2004**, *14*, 173.
(32) Starr, T. E.; Thompson, N. L. *J. Phys. Chem. B* **2002**, *106*, 2365.
(33) Brenner, H. *Chem. Eng. Sci.* **1961**, *16*, 242.

(34) Russel, W. B.; Saville, D. A.; Schowalter, W. R. *Colloidal Dispersions*; Cambridge University Press: Cambridge, United Kingdom, 1989; Chapters 2−4.

(35) Forsten, K. E.; Lauffenburger, D. A. *J. Comput. Biol.* **1994**, *1*, 15.

(36) Frej, N. A.; Prieve, D. C. *J. Chem. Phys.* **1993**, *98*, 7552.

(37) Bevan, M. A.; Prieve, D. C. *J Chem Phys.* **2000**, *113*, 1228.

(38) Lin, B.; Yu, J.; Rice, S. A. *Phys. Rev. E* **2000**, *62*, 3909.

(39) Dufresne, E. R.; Squires, T. M.; Brenner, M. P.; Grier, D. G. *Phys. Rev. Lett.* **2000**, *85*, 3317.

(40) Pagac, E. S.; Tilton, R. D.; Prieve, D. C. *Chem. Eng. Commun.* **1996**, *150*, 105.

(41) Pralle, A.; Florin, E. L.; Stelzer, E. H. K.; Horber, J. K. H. *Appl. Phys. A: Mater. Sci. Process.* **1998**, *66*, S71.

(42) Sholl, D. S.; Fenwick, M. K.; Atman, E.; Prieve, D. C. *J. Chem. Phys.* **2000**, *113*, 9268.

(43) Oetama, R. J.; Walz, J. Y. *J. Colloid Interface Sci.* **2005**, *284*, 323.

(44) Thompson, N. L.; Pero, J. K. Total internal reflection fluorescence microscopy: Applications in biophysics. In *Fluorescence Spectroscopy in Biology: Advanced Methods and Their Applications to Membranes, Proteins, DNA and Cells*; Wolfbeis, O. S., Hof, M., Hutterer, R., Fidler, V., Eds.; Springer-Verlag: Berlin, 2005; pp 79−103.

(45) Thompson, N. L.; Pero, J. K. Total internal reflection−fluorescence correlation spectroscopy. In *Reviews in Fluorescence*; Geddes, C. D., Lakowicz, J. R., Eds.; Kluwer Academic/Plenum Press: New York, in press.

(46) Abramowitz, M.; Stegun, I. *Handbook of Mathematical Functions*; Dover Publications: New York, 1968; pp 297−329.

(47) Thompson, N. L. Fluorescence correlation spectroscopy. In *Topics in Fluorescence Spectroscopy*; Lakowicz, J. R., Ed.; Plenum Press: New York, 1991; Vol. 1, pp 337−378.

(48) Poglitsch, C. L.; Thompson, N. L. *Biophys. J.* **1990**, *57*, A292.

(49) Lagerholm, B. C.; Starr, T. E.; Volovyk, Z. N.; Thompson, N. L. *Biochemistry* **2000**, *39*, 2042.

(50) Starr, T. E.; Thompson, N. L. *Langmuir* **2000**, *16*, 10301.

(51) Thompson, N. L.; Pearce, K. H.; Hsieh, H. V. *Eur. Biophys J.* **1993**, *22*, 367.

(52) Hillesheim, L. N.; Müller, J. D. *Biophys J.* **2005**, *89*, 3491.

(53) Allen, N. W.; Thompson, N. L. *Cytometry*, in press.

(54) Armstrong, J. K.; Wenby, R. B.; Meiselman, H. J.; Fisher, T. C. *Biophys. J.* **2004**, *87*, 4259.

(55) Taylor, J. R. *An Introduction to Error Analysis: The Study of Uncertainties in Physical Measurements*, 2nd ed.; University Science Books: Sausalito, CA, 1997.

(56) Weissman, M. B.; Pan, R. C.; Ware, B. R. *J. Chem. Phys.* **1979**, *70*, 2897.

(57) Gaigalas, A. K.; Hubbard, J. B.; McCurley, M.; Woo, S. *J. Phys. Chem.* **1992**, *96*, 2355.

(58) Kuehner, D. E.; Heyer, C.; Ramsch, C.; Fornefeld, U. M.; Blanch, H. W.; Prausnitz, J. M. *Biophys. J.* **1997**, *73*, 3211.

(59) Le Bon, C.; Nicolai, T.; Kuil, M. E.; Hollander, J. G. *J. Phys. Chem. B* **1999**, *103*, 10294.

(60) Beretta, S.; Chirico, G.; Baldini, G. *Macromolecules* **2000**, *33*, 8663.

(61) Bowen, W. R.; Liang, Y. C.; Williams, P. M. *Chem. Eng. Sci.* **2000**, *55*, 2359.

(62) Grigsby, J. J.; Blanch, H. W.; Prausnitz, J. M. *J. Phys. Chem. B* **2000**, *104*, 3645.

(63) Kask, P.; Palo K. Introduction to the theory of fluorescence intensity distribution analysis. In *Fluorescence Correlation Spectroscopy: Theory and Applications*; Rigler, R., Elson, E, L., Eds.; Springer-Verlag: Berlin, 2001; pp 438−458.

(64) Thompson, N. L.; Mitchell. J. L. High order autocorrelation in fluorescence correlation spectroscopy. In *Fluorescence Correlation Spectroscopy: Theory and Applications*; Rigler, R., Elson, E. L., Eds.; Springer-Verlag: Berlin, 2001; pp 438−458.

(65) Mashanov, G. I.; Tacon, D.; Peckman, M.; Molloy, J. E. *J. Biol. Chem.* **2004**, *279*, 15274.

(66) Ueda, M.; Sako, Y.; Tanaka, T.; Devreotes, P.; Yanagida, T. *Science* **2001**, *294*, 864.